

# Generating Person-Scene Interactions in 3D Scenes

Siwei Zhang<sup>1</sup> Yan Zhang<sup>1</sup> Qianli Ma<sup>2</sup> Michael J. Black<sup>2</sup> Siyu Tang<sup>1</sup>

<sup>1</sup>ETH Zürich <sup>2</sup>Max Planck Institute for Intelligent Systems

{siwei.zhang, yan.zhang, siyu.tang}@inf.ethz.ch {qma, black}@tue.mpg.de



Figure 1: Given a 3D scene mesh, our method generates human-scene proximal relations and infers a plausible human body. The selected local scene vertices are denoted by spheres, and the color denotes the generated minimum distance to the body mesh. Distances are normalized to  $[0, 1]$  for visualization, and red to purple means close to far.

## Abstract

High fidelity digital 3D environments have been proposed in recent years; however, it remains extreme challenging to automatically equip such environment with realistic human bodies. Existing work utilizes images, depths, or semantic maps to represent the scene, and parametric human models to represent 3D bodies in the scene. While being straightforward, their generated human-scene interactions are often lack of naturalness and physical plausibility. Our key observation is that humans interact with the

world through body-scene contact. To explicitly and effectively represent the physical contact between the body and the world is essential for modeling human-scene interaction. To that end, we propose a novel interaction representation, which explicitly encodes the proximity between the human body and the 3D scene around it. Specifically, given a set of basis points on a scene mesh, we leverage a conditional variational autoencoder to synthesize the distance from every basis point to its closest point on a human body. The synthesized proximal relationship between the human body and the scene can indicate which region a person tends

*to contact. Furthermore, based on such synthesized proximity, we can effectively obtain expressive 3D human bodies that naturally interact with the 3D scene. Our perceptual study shows that our model significantly improves the state-of-the-art method, approaching the realism of real human-scene interaction. We believe our method makes an important step towards the fully automatic synthesis of realistic 3D human bodies in 3D scenes. Our code and model will be publicly available for research purpose.*

## 1. Introduction

Automated synthesis of realistic humans posed naturally in a 3D scene is essential for many applications, such as VR/AR, video games, special movie effect and synthetic dataset generation for machine learning algorithms. To achieve high realism, manual animation of the human-scene interaction is often required. Recent works [21, 42] have proposed methods for the fully automated generation of human bodies that interact with the 3D world, and yet the naturalness and the realism of their results are still far behind the captured real human-scene interaction such as [14].

The main reason is that current approaches lack an explicit interaction representation. Humans interact with the 3D scene through *contact*. Explicitly exploiting the contact relations between the body and the scene is key to the realism of the synthesized humans in the scene. However, existing methods use images, semantic, and depth maps to represent the 3D environment [21, 42]. While being easily incorporated into deep convolutional networks, the 3D scene structure and the proximity between the body and the scene are not explicitly modeled, especially for the regions occluded from the camera view, making it hard to effectively enforce constraints in 3D, such as no inter-penetration and proper contact. Without a realistic contact relation, the naturalness and the physical plausibility of the synthesized human bodies are hardly guaranteed.

To address these problems, in this paper we propose explicit representations for the 3D scene and the person-scene contact relation in a coherent manner. Inspired by the Basis Point Set (BPS) method [29], which efficiently represents a 3D human body by its minimum distances to a set of random points, we propose a *two-stage* BPS encoding scheme: provided a fixed set of random basis points, we first compute the minimum distances from the basis points to the scene mesh vertices, and use this distance-based feature to represent the 3D scene. Furthermore, we use these selected scene vertices to compute the minimum distances to the body mesh, and use this distance-based feature to represent the person-scene interaction. Consequently, the scene representation and the person-scene interaction representation have a fixed dimension regardless of various scene structures and the body poses. Note that, our distance-based

interaction representation explicitly describes the contact and the proximal relations between the human body and the scene, and can be regarded as the scene ‘affordance’. Compared to other person-scene interaction representations [7, 30, 31, 32, 34], our method is purely geometry-based, is more efficient than the dense affordance map, and requires neither scene semantics nor action type labeling, nor affordance class annotations.

With our novel person-scene representation and the 3D scene encoding scheme, we train a conditional variational autoencoder (cVAE) to generate the plausible contact and proximal relations between the human body and the scene. Afterwards, from the generated interaction representation as well as the 3D scene mesh vertices, we use a regressor to recover a plausible full body mesh, which fits the generated proximal relation, and is naturally posed in the scene. Following [14, 42], we further refine the body mesh via optimization; going beyond prior work, we introduce a novel objective term based on our interaction representation that further improve the performance.

We evaluate the performance of our method on three datasets: **PROX** [14], **MP3D** [2, 42], and **Replica** [37], with a variety of metrics, namely diversity, physical plausibility, and perceptual naturalness. Experiments show that our method outperforms state-of-the-art methods [21, 42]. Particularly, the extensive perceptual studies demonstrate that our method significantly improves the naturalness and the realism of the synthesized human-scene interaction, making an important step towards the fully automatic generation of realistic human bodies in a 3D environment.

We summarize our contributions as follows: (1) We propose a novel human-scene interaction representation that is efficient, compact and consistent across various bodies and scene structures. (2) We learn a generative model for our interaction representation, that is able to synthesize full human body meshes in unknown scenes with natural poses and plausible contact relations. (3) We show through comprehensive experiments that our method achieves the new state-of-the-art performance, without using other modalities that are required in prior works [21, 42], such as depths and mesh semantics.

## 2. Related Work

**2D human-object interaction.** Perceiving human-object interactions in 2D images have been studied in many works, e.g. [5, 9, 10, 15, 16, 22, 23, 24, 35, 39, 40, 43]. Gkioxari et al. [10] detect (human, verb, object) triplets using human appearance as cues to localize interacted objects. Fang et al. [9] learn a pairwise body-part attention model, which focuses on crucial body parts and their corresponding interactions. Wang et al. [39] predict interaction points to localize and classify the interaction directly. Li et al. [22] learn a joint 2D-3D representation by estimating 3D human

pose and interacted object position. Besides detecting interactions, generating objects with natural interactions in 2D images is also studied. Tan et al. [38] learn a human instance composition model, which selects and transforms a human to an input image background. Lee et al. [20] insert an object or human instance mask into the semantic map of an image, and predicts the shape and pose of the object mask. Dvornik et al. [8] predict which object is suitable to be placed in a given region in the image as a data augmentation method.

**3D human-scene interaction.** The human-scene interaction in 3D has been widely studied in the literature, e.g. in [1, 11, 13, 17, 33, 34, 44]. Savva et al. [34] learn a joint distribution of human poses and object structures, and generate plausible human body poses and object arrangements given the action. Gupta et al. [13] propose a human-centric scene representation to model physical interactions between the body and the given indoor scene, to predict human poses supported by the scene geometry. Kim et al. [17] predict a human pose on a given 3D object, by learning an affordance model for a class of shapes. Grabner et al. [11] learn an affordance detector to identify regions in a 3D scene that supports a particular functional category such as ‘sitting’. Zhu et al. [44] infer forces or pressures applied on the body parts interacting with the scene and learn comfort intervals through physical simulation. Monszpart et al. [26] recover both a plausible scene arrangement and human motions to fit an input monocular video by jointly reasoning about scene objects and human motions over space-time. Chen et al. [4] jointly learn scene parsing, object bounding-boxes, camera pose, room layout and 3D human pose estimation given a single-view image. Li et al. [21] learn a 3D pose generative model automatically putting 3D body skeletons into the input scene represented by RGB, RGB-D, or depth image. Cao et al. [1] predict 3D human paths and pose sequences given a scene image and 2D pose histories. Most similar to our work, recently Zhang et al. [42] propose a cVAE to generate 3D human mesh modeled by SMPL-X [28] model given a 3D environment represented by an RGB-D image.

**Ours versus related work.** Compared to previous work, we explicitly use the proximity to model human-scene interaction in 3D. With this compact representation, we train a cVAE from real human-scene interaction data to synthesize the proximal relations between the human body and the scene. We show significant improvement on a large-scale perceptual study. The results indicate that our method is approaching the realism of real human-scene interaction.

### 3. Methods

#### 3.1. Scene-Body Interaction Representation

We use the Basis Point Sets (BPS) method [29] to represent the scene, the human body, and their interactions. The BPS method encodes a 3D object into a feature vector defined on a fixed set of randomly selected basis points. This feature vector, e.g. the distances from the basis points to their nearest neighbors on the target object, essentially captures their proximity relation. Such property is well in line with our objective: by selecting basis points on the scene mesh, this distance-based feature naturally represents the body-scene contact relation. However, we find the derived BPS feature is sensitive to basis point permutations, and cannot be generalized to new scenes. To address these issues, we propose a *two-stage* BPS method that encodes the scene and the body consecutively (see Fig. 2).

**Stage 1: BPS encoding for 3D Scene.** To represent a 3D scene, we follow [29] and create a set of  $N = 10^4$  uniformly random basis points  $\mathcal{V}_o \subset \mathbb{R}^{N \times 3}$  within a unit sphere.  $\mathcal{V}_o$  is kept fixed throughout the pipeline for all scenes. The scene meshes are also normalized into the unit sphere. Then, for each basis point in  $\mathcal{V}_o$ , we find its nearest neighbor in the normalized scene mesh vertices, select the corresponding scene vertex and compute the distance. Such minimum distances form the *scene feature*  $\mathbf{x}_s \in \mathbb{R}^{N \times 1}$ , and the selected  $N$  scene vertices,  $\mathcal{V}_s \subset \mathbb{R}^{N \times 3}$ , will serve as *scene BPS* to encode the body in the second stage.

In practice, only the part of the scene that is close to the human body is most relevant for modeling the interaction. This motivates us to consider ‘local scenes’, i.e. encode only part of the scene surrounding the body. To do so, we specify a virtual 3D cage around the body, and only consider the scene vertices within the cage. Furthermore, we regularly sample points on the top and the 4 side faces of the cage, and consider them as the ‘ceiling’ and ‘walls’ of the local scene. The local scene then goes through the encoding pipeline described above. We find the inclusion of the virtual ceiling and walls useful in many cases, as otherwise the scene BPS  $\mathcal{V}_s$  can fail to capture the full human body. For example, in the simplest configuration where the human stands in a 3D environment that only consists of a floor, without the virtual ceiling and the walls,  $\mathcal{V}_s$  only consists of the vertices on the floor, then the body, except the feet, will hardly be encoded by the scene BPS.

**Stage 2: BPS encoding for 3D Body.** The obtained scene BPS  $\mathcal{V}_s$ , which also includes vertices on the cage surfaces, is employed to encode the body mesh, following the same nearest neighbor encoding pipeline. We use the SMPL-X [28] model to represent the 3D human body as a mesh with vertices  $\mathcal{V}_b \subset \mathbb{R}^{10475 \times 3}$ . The BPS encoding compresses  $\mathcal{V}_b$  into the *body feature*,  $\mathbf{x}_b \in \mathbb{R}^{N \times 1}$ , which is obtained by computing the distance between each point in scene BPS to

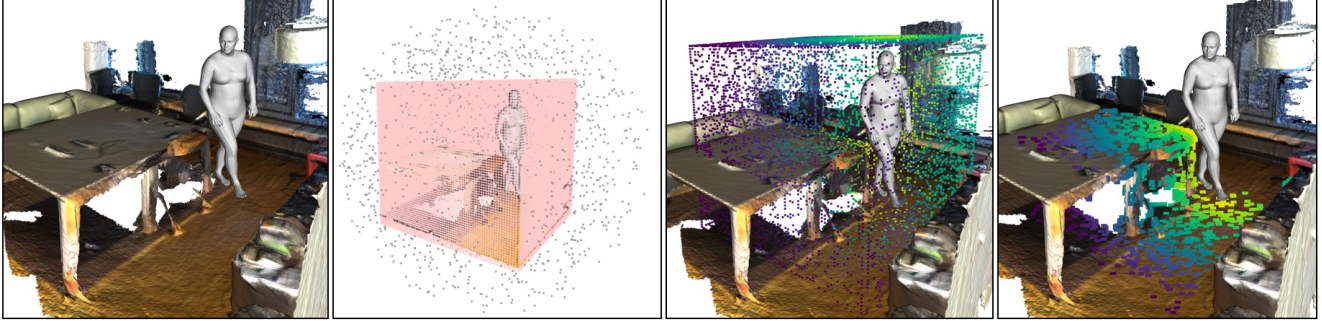


Figure 2: Illustration of human-scene interaction feature extraction (Sec. 3.1). From left to right: (1) A pair of human-scene meshes from the **PROX** dataset [14]. (2) The cropped scene mesh as well as the 3D cage (in pink) are normalized into the unit sphere. (3) The derived scene BPS  $\mathcal{V}_s$  is denoted by colored points, and the color indicates the distance-based body BPS features, i.e. the minimum distance from each scene basis point to the body mesh vertices. Small to large distance is denoted by bright yellow to dark purple. (4) The scene BPS and their minimum distances to the body only on the original scene mesh.

its nearest point of the body mesh vertices. The proposed *body feature* is scene dependent, which explicitly encodes the contact and the proximal relations between the human body and the scene, and can be used to as the interaction representation to model and synthesize realistic human bodies in the 3D scene.

It is noticed that the basis points in the unit sphere are always fixed. Consequently, each basis point in the unit sphere always corresponds to a basis point on the scene mesh, and every dimension in the scene feature always corresponds to the same dimension in the body feature. Such scene-body representation is hence consistent across various human body poses and scene structures.

### 3.2. Scene-Body Interaction Generator

Provided a pair of interacting body mesh and scene mesh, we are able to derive the scene BPS  $\mathcal{V}_s$ , the scene feature  $\mathbf{x}_s$ , and the body feature  $\mathbf{x}_b$ . Therefore, when provided a number of such triplets as training samples, we can learn a generative model, so as to infer plausible human-scene contact and proximal relations in the scene and recover full human body meshes.

#### 3.2.1 Network Architecture

The network architecture is illustrated in Fig. 3. The entire network incorporates a conditional variational autoencoder (cVAE) [19, 36] to generate body features based on a scene feature auto-encoder  $E$ , and a multilayer perceptron  $H$  as a regressor to produce full body meshes, based on the reconstructed body features and the scene BPS auto-encoder  $F$ . We denote the downstream cVAE network as  $G$ . Intermediate features from the decoder in  $E$  are introduced to the decoder in  $G$  for better scene conditioning (please refer to the appendix for its ablation study). Details of the network architecture are demonstrated in the appendix.

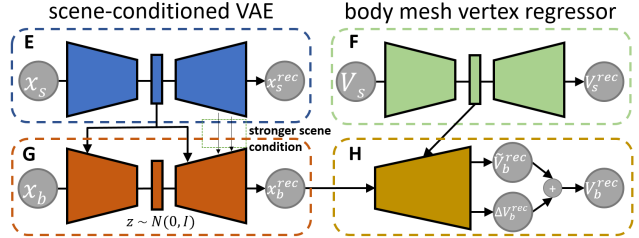


Figure 3: Illustration of the generator architecture.  $\mathbf{x}_s$ ,  $\mathcal{V}_s$ ,  $\mathbf{x}_b$  and  $\mathcal{V}_b$  denote the scene feature, the scene BPS, the body feature, and the full body mesh vertices. Also,  $\Delta\mathcal{V}_b^{rec}$  denotes a global 3D translation, which is to shift the intermediate produced body vertices. Note that all point coordinates are relative to the center of the normalized 3D cage in the unit sphere. The optional “stronger scene condition” is to introduce additional intermediate features to the VAE decoder. Best viewed zoomed on a color screen.

#### 3.2.2 Training Loss

All the network modules are jointly trained end-to-end. Following Sec. 3.1, we can obtain a set of representations from each ground truth sample, namely  $\{\mathbf{x}_s, \mathbf{x}_b, \mathcal{V}_s, \mathcal{V}_b\}$  denoting the scene feature, the body feature, the scene BPS, and the full body vertices, respectively. It is noted that the point coordinates are rescaled in the unit sphere, and relative to the rescaled 3D cage center. We denote the operations of transforming from the rescaled 3D cage back to the original world as  $\pi(\cdot)$ , and its inverse operation as  $\pi^{-1}(\cdot)$ . The training loss is given by

$$\mathcal{L} = \mathcal{L}_{rec} + \alpha_1 \mathcal{L}_{KL} + \alpha_2 \mathcal{L}_{coll} + \alpha_3 \mathcal{L}_{contact}, \quad (1)$$

in which  $\{\alpha_1, \alpha_2, \alpha_3\}$  are loss weights as hyper-parameters.

**Reconstruction term:** This term is given by

$$\mathcal{L}_{rec} = |\mathbf{x}_s - \mathbf{x}_s^{rec}| + |\mathbf{x}_b - \mathbf{x}_b^{rec}| + |\mathcal{V}_b - \tilde{\mathcal{V}}_b^{rec}|, \quad (2)$$

in which the last term denotes vertex-wise reconstruction.

**KL-divergence term:** Following [19], we specify the latent prior as the standard normal distribution, and employ the same re-parameterization approach to model the inference posterior  $q(\mathbf{z}|\mathbf{x})$ . To effectively avoid posterior collapse, we use the robust KL-divergence term as in [41]. Our KL-divergence term is given by

$$\mathcal{L}_{KL} = \Psi(q(\mathbf{z}|\mathbf{x})||\mathcal{N}(0, \mathbf{I})), \quad (3)$$

in which  $\Psi(\cdot)$  is the Charbonnier function  $\Psi(s) = \sqrt{s^2 + 1} - 1$  [3]. According to [41], the smaller is the KL-divergence between the inference posterior and the prior, the smaller are the gradients to update this KL-divergence.

**The collision term and the contact term:** As in [42], these two terms are given by

$$\mathcal{L}_{coll} = \frac{1}{|\mathcal{V}_b|} \sum_{\mathbf{v}_b \in \pi(\mathcal{V}_b^{rec})} |\Phi^-(\mathbf{v}_b)|, \quad (4)$$

$$\mathcal{L}_{contact} = \sum_{\mathbf{v}_b \in C(\pi(\mathcal{V}_b^{rec}))} \min_{\mathbf{v}_s \in \mathcal{M}_s} \rho(|\mathbf{v}_b - \mathbf{v}_s|), \quad (5)$$

in which  $C(\cdot)$  denotes the mask to select the body part for contact,  $|\mathcal{V}_b|$  denotes the constant number of the body mesh vertices,  $\Phi^-(\cdot)$  is the scene negative signed distance field (SDF),  $\mathcal{M}_s$  is the provided scene mesh, and  $\rho(\cdot)$  is the Geman-McClure error function to remove the influence of scene mesh vertices far away from the body [14, 42]. In contrast to [14, 42], the contact mask  $C(\cdot)$  only considers feet, which we find is better to avoid body floating.

### 3.2.3 Generating 3D Human in the Scene

During testing, only the 3D scene mesh is needed. The generation procedures are: (1) We randomly create a 3D cage within the scene and transform it into the pre-defined unit sphere. (2) Within the unit sphere, we compute the scene BPS  $\mathcal{V}_s$  and the scene feature  $\mathbf{x}_s$ . (3) Our cVAE is employed to generate a body feature  $\mathbf{x}_b$ . (4) Based on  $\mathcal{V}_s$  and  $\mathbf{x}_b$ , the regressor is employed to produce a set of body mesh vertices, which is then transformed back to the original world.

### 3.3. Interaction-based Optimization

The body vertices produced by the regressor are not guaranteed to form a valid body shape: The raw output from the network can suffer from noisy surface geometry or inter-penetration with the scene. Therefore, we conduct an additional optimization step to convert the regressed body mesh

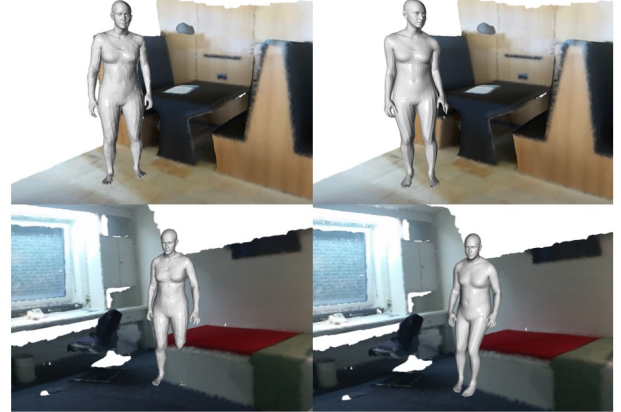


Figure 4: Illustration of optimization results. The left column shows two generated body mesh vertices, and the right column shows their optimized results.

vertices to a SMPL-X body mesh. Given the scene mesh  $\mathcal{M}_s$ , the body feature  $\mathbf{x}_b$ , and the regressed body mesh vertices  $\mathcal{V}_b$ , the optimization loss is given by

$$\begin{aligned} \mathcal{L}(\theta) = & |\pi(\mathcal{V}_b) - \mathcal{V}_{SMPLX}(\theta)| + |\mathbf{x}_b - f(\pi^{-1}(\mathcal{V}_{SMPLX}(\theta)))| \\ & + \lambda_1 \mathcal{L}_{coll} + \lambda_2 \mathcal{L}_{contact} + \lambda_3 \mathcal{L}_{vposer} \\ & + \lambda_4 \mathcal{L}_{hand} + \lambda_5 \mathcal{L}_{shape}, \end{aligned} \quad (6)$$

in which  $\mathcal{V}_{SMPLX}(\theta)$  denotes vertices of the SMPL-X body mesh with the attribute  $\theta$  (including global translation, orientation, body shape, pose and hand pose),  $\mathcal{L}_{coll}$  and  $\mathcal{L}_{contact}$  are the same in Eq. (4). In addition,  $\mathcal{L}_{vposer}$ ,  $\mathcal{L}_{hand}$ ,  $\mathcal{L}_{shape}$  are the VPoser loss [14, 28], L2 prior loss for hand and shape parameters in SMPL-X model to ensure natural body, hand poses and shapes of the optimized body, respectively.  $\lambda$ 's are loss weights as hyper-parameters, and  $f(\cdot)$  is the operation to extract the body feature from the body mesh, demonstrated in Sec. 3.1.

In the optimization loss, the first term denotes the vertex-wise reconstruction, in order to discourage dramatic deviation of the resultant SMPL-X body mesh from the regressed body vertices. Additionally, we employ the second term to encourage the resultant SMPL-X body mesh to have the same contact relation with the scene. Unlike the heuristic contact term  $\mathcal{L}_{contact}$ , this BPS feature reconstruction term is data-driven, since the body feature can be learned from data and generated by our cVAE model.

Fig. 4 shows two results of optimization. We can see that the human-scene contact is preserved, and their inter-penetration is considerably alleviated.

## 4. Experiments

### 4.1. Datasets

**PROX** [14]. This dataset includes 12 different room 3D scans, and captures natural actions of 20 subjects, which are represented by SMPL-X body meshes [28]. Following [42], we select ‘MPH1Library’, ‘MPH16’, ‘N0SittingBooth’ and ‘N3OpenArea’ for testing, and use the rests for training, from which we extract interaction features from 63,599 human-scene pairs. To improve generalization to new scenes, we perform data augmentation<sup>1</sup> 4 times for each human-scene pair, and obtain 254,396 training samples in total. During testing, we randomly set 1200 3D cages in each test scene, and generate one random sample in each cage. This results in 4800 examples for evaluation.

**MP3D** [2]. This dataset has 90 building-scale scene scans with semantic annotations. Following the setup in [42], we perform testing on the same 7 scenes with corresponding scene SDFs, and generate the same number of random samples for each scene as in [42], which is hence 6400 random samples in total.

**Replica** [37]. This dataset contains reconstructed indoor scenes of clean dense geometry, with semantic and instance segmentation annotations. Replica includes 18 scenes of 5 different room types, among which we select 1 room in each type, resulting in 5 rooms (‘office\_2’, ‘hotel\_0’, ‘room\_0’, ‘frl\_apartment\_0’, ‘apartment\_1’) for testing. 1200 random samples are generated on each scene for evaluation.

### 4.2. Our method and Baselines

In this paper, we denote our model trained without  $\mathcal{L}_{\text{coll}}$  and  $\mathcal{L}_{\text{contact}}$  as Ours. Its ablation study is referred to Sec. 4.6 and appendix. We compare our method with two baselines: (1) PSI [42], which generates SMPL-X parameters given the scene depth and the semantic segmentation. Specifically, we perform comparison with their S1 model without the human-scene interaction training loss, both before and after the geometry-aware fitting, which are reported to outperform other methods. (2) Li et al. [21], which generates 3D body sticks based on scene appearance and depth. We perform comparison with its modified version proposed in [42], which generates SMPL-X parameters for a fair comparison.

It is noted that these two baselines generate SMPL-X parameters, yet our method directly produces body vertices, which might not form a valid body shape. To fairly compare with baselines before their geometry-aware fitting, we perform an optimization step to derive SMPL-X parameters from the body vertices, for which  $\mathcal{L}_{\text{contact}}$  and  $\mathcal{L}_{\text{coll}}$  in Eq. 6 are excluded. We denote this optimization as SimOptim, and the optimization with all terms as AdvOptim in the following

<sup>1</sup>See data preprocessing and augmentation details in the Appendix.

Table 1: **Unary user study.** We calculate the results from all turkers, and report the the scores w.r.t. the average  $\pm$  the standard deviation. Best results except the ground truth are shown in boldface.

model	PROX	MP3D
Li et al. [21] + $\mathcal{L}_f$	$3.37 \pm 1.31$	$3.52 \pm 1.34$
PSI [42] + $\mathcal{L}_f$	$3.47 \pm 1.27$	$3.23 \pm 1.40$
Ours + $\mathcal{L}_{\text{contact}}$ + SimOptim	$3.61 \pm \mathbf{1.16}$	$3.77 \pm 1.15$
Ours + $\mathcal{L}_{\text{contact}}$ + AdvOptim	$\mathbf{3.71} \pm 1.17$	$\mathbf{3.84} \pm \mathbf{1.11}$
Ground truth	$3.94 \pm 0.99$	–

content. Moreover, we denote the scene geometry-aware fitting proposed in [42] as  $\mathcal{L}_f$ .

### 4.3. Quantitative Evaluation

We evaluate the performance in terms of perceptual naturalness, diversity, and physical plausibility, following Zhang et al. [42].

#### 4.3.1 Perceptual Naturalness

We run user studies on Amazon Mechanical Turk (AMT), and use two protocols to perform comparison. For each scene and each model, we generate 100 and 400 examples for **PROX** and **MP3D**, respectively, as in [42].

**Unary user study.** Like [42], we ask turkers to evaluate each individual generated result or ground truth, giving a score from 1 (strongly not natural) to 5 (strongly natural). Each result is rated by 3 turkers. The results are shown in Tab. 1. On both **PROX** and **MP3D**, our methods with SimOptim and AdvOptim both outperform baseline methods after their geometry-aware fitting.

**Binary user study.** To perform a direct comparison, we follow [21, 25], and show results of two methods to the turkers at the same time. The turkers are asked to pick the one that they think is more perceptually natural. For **PROX**, we compare the best instance of our method (the one trained with  $\mathcal{L}_{\text{contact}}$  and AdvOptim) against [42] with the geometry-aware fitting  $\mathcal{L}_f$ , and against the ground truth, respectively. For **MP3D**, we compare with [42] with  $\mathcal{L}_f$ .

As shown in Tab. 2, Our method outperforms PSI [42] on both datasets by a large margin. More interestingly, in the direct comparison with the **PROX** ground truth, our generated results are regarded as more realistic by nearly half (48.5%) of the users, indicating that our results are hardly distinguishable from the real human-scene interaction. It suggests that our method makes an important step towards the fully automatic synthesis of realistic 3D human bodies in 3D scenes.

Table 2: **Binary user study.** Numbers show the percentage of the users that rate the corresponding method as more realistic.

Datasets	% users rated as “better”	
<b>MP3D</b>	Ours + $\mathcal{L}_{\text{contact}} + \text{AdvOptim}$	PSI + $\mathcal{L}_f$ <b>70.1%</b> 29.9%
<b>PROX</b>	Ours + $\mathcal{L}_{\text{contact}} + \text{AdvOptim}$	PSI + $\mathcal{L}_f$ <b>69.0%</b> 31.0%
<b>PROX</b>	Ours + $\mathcal{L}_{\text{contact}} + \text{AdvOptim}$	GT 48.5% <b>51.5%</b>

### 4.3.2 Diversity

**Evaluation metrics.** Like [42], we perform K-means to cluster the SMPL-X parameters of generated bodies into 20 clusters for each test scene, and evaluate the model by: 1) the entropy of the cluster ID histogram for all samples, and 2) the cluster size, which denotes the average distance between the sample and the corresponding cluster center. The higher, the better for both metrics. We report average scores for all test scenes.

**Results.** Tab. 3 presents the diversity results. Comparing with baselines, Ours+ $\mathcal{L}_{\text{contact}} + \text{SimOptim}$  achieve comparable entropy and cluster size on both **PROX** and **MP3D**. When applying AdvOptim, the cluster size is further increased by a large margin, indicating that the generated bodies are more scattered in the scene. Since the cluster size is correlated with the test scene size, its values are higher on **MP3D** and **Replica** than **PROX** due to larger room sizes.

### 4.3.3 Physical Plausibility

**Evaluation metrics.** We evaluate the non-collision and contact scores between the generated body and scene mesh, following the metrics in [42]. Specifically, the non-collision score is the ratio of the number of body vertices with non-negative scene SDF values to the number of all body vertices (10475). The contact score is 1 if any body mesh vertex has a non-positive scene SDF value, otherwise 0. Then we report the average non-collision scores and average contact scores of all test examples. Thus, a higher non-collision score indicates fewer body-scene inter-penetrations, while a higher contact score suggests more contacts between the generated body and scene mesh. Higher values for both scores are desirable.

**Results.** Tab. 3 shows the results of physical plausibility. On **PROX**, Ours+ $\mathcal{L}_{\text{contact}} + \text{SimOptim}$  achieves higher non-collision score and comparable contact score with the baselines, indicating that our proposed method can effectively alleviate scene-body inter-penetration, while preserv-



Figure 5: Generated results in **PROX**, **MP3D** and **Replica** datasets.

ing plausible contact relations. When additionally employing the interaction-based optimization, performance is further consistently improved. In addition, we find the SDFs on **MP3D** are not sufficiently reliable probably due to noisy scans<sup>2</sup>. Thus, we further perform evaluation on the **Replica** dataset, from which high-quality scene SDFs can be derived. The results on **Replica** verify the effectiveness of our model, which is consistent with the performances on **PROX**.

## 4.4. Qualitative Results.

Fig. 5 shows some generated human bodies in the three datasets. To further analyze our cVAE, we perform interpolation in its latent space, and show the results in Fig. 6. We can see that the body changes smoothly, while preserving natural interactions with the scene. Note that the results in Fig. 6 are directly produced by the body vertex regressor  $H$ , without any optimization-based refinement.

## 4.5. Limitation and Failure Cases

Despite the effectiveness verified by our evaluations, our method still have limitations. For example, the generated body might inter-penetrates with a thin structure in the scene mesh, e.g. the table surface. In this case, AdvOptim cannot resolve this issue, since the value of the collision loss  $\mathcal{L}_{\text{coll}}$  is already very small. We thus expect a novel collision representation in future could resolve this issue. Furthermore, detailed and diverse hand poses can not be well synthesized by the current model. Because the basis point set on the scene mesh are too sparse to model the hand-object interaction. We expect a coarse-to-fine encoding scheme could help. We consider these challenges as exciting future directions. Visualizations of the failure cases can be found in the Appendix.

## 4.6. Ablation Study

We investigate the influence of the training loss and the optimization scheme on our model performance on **PROX**

<sup>2</sup>Illustrations are presented in the Appendix.

Table 3: **Evaluation on diversity and physical plausibility:** For the entropy, the cluster size, the non-collision score and the contact score, their values are the higher, the better. Row-wisely, the first part and the second part show the comparison to baseline methods before and after geometry-aware fitting, respectively. For each part, the best results are in boldface.

Methods	Diversity						Physical plausibility					
	entropy			cluster size			non-coll			contact		
	PROX	MP3D	Replica	PROX	MP3D	Replica	PROX	MP3D	Replica	PROX	MP3D	Replica
Li et al. [21]	2.86	2.90	-	1.21	1.71	-	0.89	0.92	-	0.93	0.78	-
PSI [42]	<b>2.95</b>	<b>2.96</b>	-	2.39	2.77	-	0.93	0.94	-	<b>0.95</b>	<b>0.80</b>	-
Ours + $\mathcal{L}_{\text{contact}}$	-	-	-	-	-	-	0.95	<b>0.97</b>	<b>0.92</b>	0.90	0.57	0.90
Ours + $\mathcal{L}_{\text{contact}}$ + AdvOptim	2.91	2.92	2.93	<b>2.47</b>	<b>2.78</b>	2.84	<b>0.96</b>	<b>0.97</b>	0.91	<b>0.95</b>	0.62	<b>0.92</b>
Li et al. + $\mathcal{L}_f$	2.86	2.92	-	1.26	1.93	-	0.93	0.97	-	<b>0.99</b>	<b>0.89</b>	-
PSI + $\mathcal{L}_f$	<b>2.95</b>	<b>2.96</b>	-	2.40	2.85	-	0.94	0.97	-	<b>0.99</b>	0.88	-
Ours + $\mathcal{L}_{\text{contact}}$ + AdvOptim	2.91	2.93	2.92	<b>2.60</b>	<b>2.96</b>	2.97	<b>0.98</b>	<b>0.98</b>	0.93	<b>0.99</b>	0.57	1.00

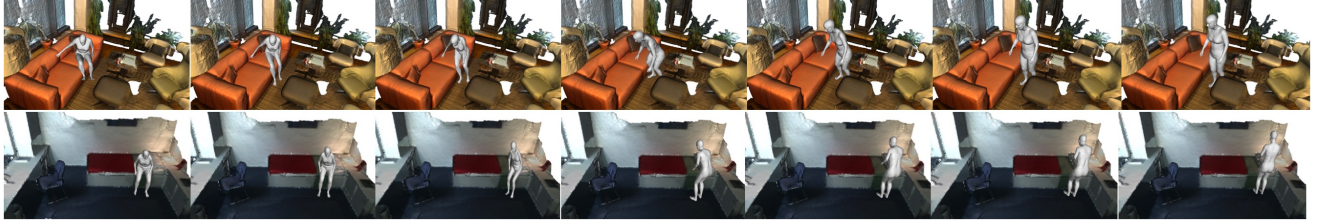


Figure 6: Latent space interpolation. In each row, the left and right images denote two different random samples, and middle images correspond to interpolated latent variables. For each row, the scene BPS  $\mathcal{V}_s$  and the scene feature  $\mathbf{x}_s$  are fixed.

Table 4: Ablation study w.r.t. diversity metrics.

Optimization	Method	entropy	cluster size
SimOptim	Ours	2.89	2.44
	Ours + $\mathcal{L}_{\text{contact}}$	<b>2.91</b>	<b>2.47</b>
	Ours + $\mathcal{L}_{\text{coll}}$	2.89	2.38
	Ours + $\mathcal{L}_{\text{contact}} + \mathcal{L}_{\text{coll}}$	2.90	2.36
AdvOptim	Ours	2.90	<b>2.60</b>
	Ours + $\mathcal{L}_{\text{contact}}$	<b>2.91</b>	<b>2.60</b>
	Ours + $\mathcal{L}_{\text{coll}}$	2.88	2.53
	Ours + $\mathcal{L}_{\text{contact}} + \mathcal{L}_{\text{coll}}$	2.89	2.48

dataset. More ablation studies are referred to the Appendix.

Tab. 4 and Tab. 5 presents model performances when trained with or without contact loss  $\mathcal{L}_{\text{contact}}$  and collision loss  $\mathcal{L}_{\text{coll}}$  in Eq. (1), respectively. We find that the model without  $\mathcal{L}_{\text{contact}}$  and  $\mathcal{L}_{\text{coll}}$  has inferior contact scores, indicating that it tends to produce more floating bodies. Also, in contrast to Zhang et al. [42], we find the loss term  $\mathcal{L}_{\text{contact}}$  is effective to improve the contact score in our model. Additionally, the model trained without  $\mathcal{L}_{\text{coll}}$  already delivers high non-collision scores, indicating the effectiveness of our BPS-based to avoid inter-penetration. However,  $\mathcal{L}_{\text{coll}}$  in training reduces the cluster size. Thus, we mostly use Ours trained with  $\mathcal{L}_{\text{contact}}$  to compare with baseline methods.

Table 5: Ablation study w.r.t. physical plausibility metrics.

Optimization	Method	non-coll	contact
w/o	Ours	<b>0.95</b>	0.83
	Ours + $\mathcal{L}_{\text{contact}}$	<b>0.95</b>	<b>0.90</b>
	Ours + $\mathcal{L}_{\text{coll}}$	<b>0.95</b>	0.83
	Ours + $\mathcal{L}_{\text{contact}} + \mathcal{L}_{\text{coll}}$	<b>0.95</b>	0.88
SimOptim	Ours	<b>0.96</b>	0.84
	Ours + $\mathcal{L}_{\text{contact}}$	<b>0.96</b>	<b>0.95</b>
	Ours + $\mathcal{L}_{\text{coll}}$	<b>0.96</b>	0.87
	Ours + $\mathcal{L}_{\text{contact}} + \mathcal{L}_{\text{coll}}$	0.95	0.94
AdvOptim	Ours	<b>0.98</b>	<b>0.99</b>
	Ours + $\mathcal{L}_{\text{contact}}$	<b>0.98</b>	<b>0.99</b>
	Ours + $\mathcal{L}_{\text{coll}}$	<b>0.98</b>	0.98
	Ours + $\mathcal{L}_{\text{contact}} + \mathcal{L}_{\text{coll}}$	<b>0.98</b>	<b>0.99</b>

Moreover, when comparing results with SimOptim and AdvOptim, we can observe that the collision and contact terms in Eq. (6) significantly improve both physical plausibility and diversity metrics, which is consistent with [42].

## 5. Conclusion

This paper introduces a novel representation to model human-scene interactions by explicitly encoding the proximity between the body and the environment. It is purely

geometry-based and consistent across various bodies and scene structures, thus only requiring the 3D mesh as the input. By training a generative model to synthesize such representations and body meshes, our approach is able to generate humans in natural interactions with new environments, which demonstrates the practical merits of our work.

**Acknowledgements.** We sincerely thank Mohamed Hassan for his scene SDF calculation protocol. This work was partially supported by the German Research Foundation (DFG): SFB 1233, Robust Vision: Inference Principles and Neural Mechanisms, TP XX, project number: 276693517. Qianli Ma acknowledges the support from the Max Planck ETH Center for Learning Systems.

**Disclosure.** MJB has received research gift funds from Intel, Nvidia, Adobe, Facebook, and Amazon. While MJB is a part-time employee of Amazon, his research was performed solely at MPI. He is also an investor in Meshcapde GmbH.

## References

- [1] Z. Cao, H. Gao, K. Mangalam, Q. Cai, M. Vo, and J. Malik. Long-term human motion prediction with scene context. 2020.
- [2] A. Chang, A. Dai, T. Funkhouser, M. Halber, M. Niessner, M. Savva, S. Song, A. Zeng, and Y. Zhang. Matterport3D: Learning from RGB-D data in indoor environments. *International Conference on 3D Vision (3DV)*, 2017.
- [3] P. Charbonnier, L. Blanc-Feraud, G. Aubert, and M. Barlaud. Two deterministic half-quadratic regularization algorithms for computed imaging. In *Proceedings of 1st International Conference on Image Processing*, volume 2, pages 168–172. IEEE, 1994.
- [4] Y. Chen, S. Huang, T. Yuan, S. Qi, Y. Zhu, and S.-C. Zhu. Holistic++ scene understanding: Single-view 3d holistic scene parsing and human pose estimation with human-object interaction and physical commonsense. In *Proceedings of the IEEE International Conference on Computer Vision*, pages 8648–8657, 2019.
- [5] V. Delaitre, J. Sivic, and I. Laptev. Learning person-object interactions for action recognition in still images. In *Advances in neural information processing systems*, pages 1503–1511, 2011.
- [6] T. Deprelle, T. Groueix, M. Fisher, V. G. Kim, B. C. Russell, and M. Aubry. Learning elementary structures for 3D shape generation and matching. In *Proceedings of the Advances in Neural Information Processing Systems (NeurIPS)*, 2019.
- [7] T.-T. Do, A. Nguyen, and I. Reid. Affordancenet: An end-to-end deep learning approach for object affordance detection. In *2018 IEEE international conference on robotics and automation (ICRA)*, pages 1–5. IEEE, 2018.
- [8] N. Dvornik, J. Mairal, and C. Schmid. On the importance of visual context for data augmentation in scene understanding. *IEEE Transactions on Pattern Analysis and Machine Intelligence*, 2019.
- [9] H.-S. Fang, J. Cao, Y.-W. Tai, and C. Lu. Pairwise body-part attention for recognizing human-object interactions. In *Proceedings of the European Conference on Computer Vision (ECCV)*, pages 51–67.
- [10] G. Gkioxari, R. Girshick, P. Dollár, and K. He. Detecting and recognizing human-object interactions. In *Proceedings of the IEEE Conference on Computer Vision and Pattern Recognition*, pages 8359–8367, 2018.
- [11] H. Grabner, J. Gall, and L. Van Gool. What makes a chair a chair? In *CVPR 2011*, pages 1529–1536. IEEE, 2011.
- [12] T. Groueix, M. Fisher, V. G. Kim, B. Russell, and M. Aubry. 3D-CODED: 3D correspondences by deep deformation. In *Proceedings of the European Conference on Computer Vision (ECCV)*, 2018.
- [13] A. Gupta, S. Satkin, A. A. Efros, and M. Hebert. From 3d scene geometry to human workspace. In *CVPR 2011*, pages 1961–1968. IEEE, 2011.
- [14] M. Hassan, V. Choutas, D. Tzionas, and M. J. Black. Resolving 3D human pose ambiguities with 3D scene constraints. In *Proceedings of the IEEE/CVF Conference on International Conference on Computer Vision (ICCV)*, pages 2282–2292, Oct. 2019.
- [15] K. Kato, Y. Li, and A. Gupta. Compositional learning for human object interaction. In *Proceedings of the European Conference on Computer Vision (ECCV)*, pages 234–251, 2018.
- [16] D.-J. Kim, X. Sun, J. Choi, S. Lin, and I. S. Kweon. Detecting human-object interactions with action co-occurrence priors. *arXiv preprint arXiv:2007.08728*, 2020.
- [17] V. G. Kim, S. Chaudhuri, L. Guibas, and T. Funkhouser. Shape2pose: Human-centric shape analysis. *ACM Transactions on Graphics (TOG)*, 33(4):1–12, 2014.
- [18] D. P. Kingma and J. Ba. Adam: A method for stochastic optimization. In Y. Bengio and Y. LeCun, editors, *3rd International Conference on Learning Representations, ICLR 2015, San Diego, CA, USA, May 7-9, 2015, Conference Track Proceedings*, 2015.
- [19] D. P. Kingma and M. Welling. Auto-encoding variational Bayes. In *Proceedings of the International Conference on Learning Representations (ICLR)*, 2014.
- [20] D. Lee, S. Liu, J. Gu, M.-Y. Liu, M.-H. Yang, and J. Kautz. Context-aware synthesis and placement of object instances. In *Advances in neural information processing systems*, pages 10393–10403, 2018.
- [21] X. Li, S. Liu, K. Kim, X. Wang, M.-H. Yang, and J. Kautz. Putting humans in a scene: Learning affordance in 3D indoor environments. In *Proceedings of the IEEE Conference on Computer Vision and Pattern Recognition (CVPR)*, 2019.
- [22] Y.-L. Li, X. Liu, H. Lu, S. Wang, J. Liu, J. Li, and C. Lu. Detailed 2d-3d joint representation for human-object interaction. In *Proceedings of the IEEE/CVF Conference on Computer Vision and Pattern Recognition*, pages 10166–10175, 2020.
- [23] Y.-L. Li, S. Zhou, X. Huang, L. Xu, Z. Ma, H.-S. Fang, Y. Wang, and C. Lu. Transferable interactiveness knowledge for human-object interaction detection. In *Proceedings of the IEEE Conference on Computer Vision and Pattern Recognition*, pages 3585–3594, 2019.
- [24] M. Liu, S. Tang, Y. Li, and J. Rehg. Forecasting human object interaction: Joint prediction of motor attention and egocentric activity. *arXiv preprint arXiv:1911.10967*, 2019.

[25] Q. Ma, J. Yang, A. Ranjan, S. Pujades, G. Pons-Moll, S. Tang, and M. J. Black. Learning to Dress 3D People in Generative Clothing. In *Computer Vision and Pattern Recognition (CVPR)*, 2020.

[26] A. Monszpart, P. Guerrero, D. Ceylan, E. Yumer, and N. J. Mitra. imapper: interaction-guided scene mapping from monocular videos. *ACM Transactions on Graphics (TOG)*, 38(4):1–15, 2019.

[27] A. Paszke, S. Gross, S. Chintala, G. Chanan, E. Yang, Z. DeVito, Z. Lin, A. Desmaison, L. Antiga, and A. Lerer. Automatic differentiation in pytorch. 2017.

[28] G. Pavlakos, V. Choutas, N. Ghorbani, T. Bolkart, A. A. A. Osman, D. Tzionas, and M. J. Black. Expressive body capture: 3D hands, face, and body from a single image. In *Proceedings of the IEEE Conference on Computer Vision and Pattern Recognition (CVPR)*, 2019.

[29] S. Prokudin, C. Lassner, and J. Romero. Efficient learning on point clouds with basis point sets. In *Proceedings of the IEEE/CVF Conference on International Conference on Computer Vision (ICCV)*, pages 4332–4341, Oct. 2019.

[30] S. Qi, Y. Zhu, S. Huang, C. Jiang, and S.-C. Zhu. Human-centric indoor scene synthesis using stochastic grammar. In *Proceedings of the IEEE Conference on Computer Vision and Pattern Recognition*, pages 5899–5908, 2018.

[31] A. Roy and S. Todorovic. A multi-scale cnn for affordance segmentation in rgb images. In *European conference on computer vision*, pages 186–201. Springer, 2016.

[32] E. Ruiz and W. Mayol-Cuevas. Geometric affordance perception: Leveraging deep 3d saliency with the interaction tensor. *Frontiers in Neurorobotics*, 14:45, 2020.

[33] M. Savva, A. X. Chang, P. Hanrahan, M. Fisher, and M. Nießner. Scenegrok: Inferring action maps in 3d environments. *ACM transactions on graphics (TOG)*, 33(6):1–10, 2014.

[34] M. Savva, A. X. Chang, P. Hanrahan, M. Fisher, and M. Nießner. Pigraphs: learning interaction snapshots from observations. *ACM Transactions on Graphics (TOG)*, 35(4):1–12, 2016.

[35] L. Shen, S. Yeung, J. Hoffman, G. Mori, and L. Fei-Fei. Scaling human-object interaction recognition through zero-shot learning. In *2018 IEEE Winter Conference on Applications of Computer Vision (WACV)*, pages 1568–1576. IEEE, 2018.

[36] K. Sohn, H. Lee, and X. Yan. Learning structured output representation using deep conditional generative models. In *Advances in neural information processing systems*, pages 3483–3491, 2015.

[37] J. Straub, T. Whelan, L. Ma, Y. Chen, E. Wijmans, S. Green, J. J. Engel, R. Mur-Artal, C. Ren, S. Verma, A. Clarkson, M. Yan, B. Budge, Y. Yan, X. Pan, J. Yon, Y. Zou, K. Leon, N. Carter, J. Briales, T. Gillingham, E. Mueggler, L. Pesqueira, M. Savva, D. Batra, H. M. Strasdat, R. D. Nardi, M. Goesele, S. Lovegrove, and R. Newcombe. The Replica dataset: A digital replica of indoor spaces. *arXiv preprint arXiv:1906.05797*, 2019.

[38] F. Tan, C. Bernier, B. Cohen, V. Ordonez, and C. Barnes. Where and who? automatic semantic-aware person composition. In *2018 IEEE Winter Conference on Applications of Computer Vision (WACV)*, pages 1519–1528. IEEE, 2018.

[39] T. Wang, T. Yang, M. Danelljan, F. S. Khan, X. Zhang, and J. Sun. Learning human-object interaction detection using interaction points. In *Proceedings of the IEEE/CVF Conference on Computer Vision and Pattern Recognition*, pages 4116–4125, 2020.

[40] B. Yao and L. Fei-Fei. Modeling mutual context of object and human pose in human-object interaction activities. In *2010 IEEE Computer Society Conference on Computer Vision and Pattern Recognition*, pages 17–24. IEEE, 2010.

[41] Y. Zhang, M. J. Black, and S. Tang. Perpetual motion: Generating unbounded human motion, 2020.

[42] Y. Zhang, M. Hassan, H. Neumann, M. J. Black, and S. Tang. Generating 3d people in scenes without people. In *Proceedings of the IEEE/CVF Conference on Computer Vision and Pattern Recognition (CVPR)*, pages 6194–6204, 2020.

[43] T. Zhou, W. Wang, S. Qi, H. Ling, and J. Shen. Cascaded human-object interaction recognition. In *Proceedings of the IEEE/CVF Conference on Computer Vision and Pattern Recognition*, pages 4263–4272, 2020.

[44] Y. Zhu, C. Jiang, Y. Zhao, D. Terzopoulos, and S.-C. Zhu. Inferring forces and learning human utilities from videos. In *Proceedings of the IEEE Conference on Computer Vision and Pattern Recognition*, pages 3823–3833, 2016.

# Generating Human-scene Interactions in 3D Scenes

## \*\*Appendix\*\*

### A. Architecture Details

The detailed architecture is illustrated in Fig. S1. During the training stage, the scene-conditioned VAE takes the body feature  $x_b$ , and reconstructs the body feature  $x_b^{rec}$  based on the scene feature  $x_s$ . Residual blocks are utilized in the scene-conditioned VAE, and the middle latent feature of the scene feature auto-encoder  $E$  is concatenated into different layers in  $G$  to enforce stronger scene conditioning. During inference, the scene-conditioned VAE generates a body feature from the randomly sampled noise  $z$  conditioned on the scene feature input  $x_s$ .

The body mesh vertex regressor includes an auto-encoder  $F$  for the scene BPS  $\mathcal{V}_s$ , and a multilayer perceptron  $H$  to reconstruct the vertex coordinates of the final body mesh.  $\Delta\mathcal{V}_b^{rec}$  denotes a global 3D translation to improve contact relationship.

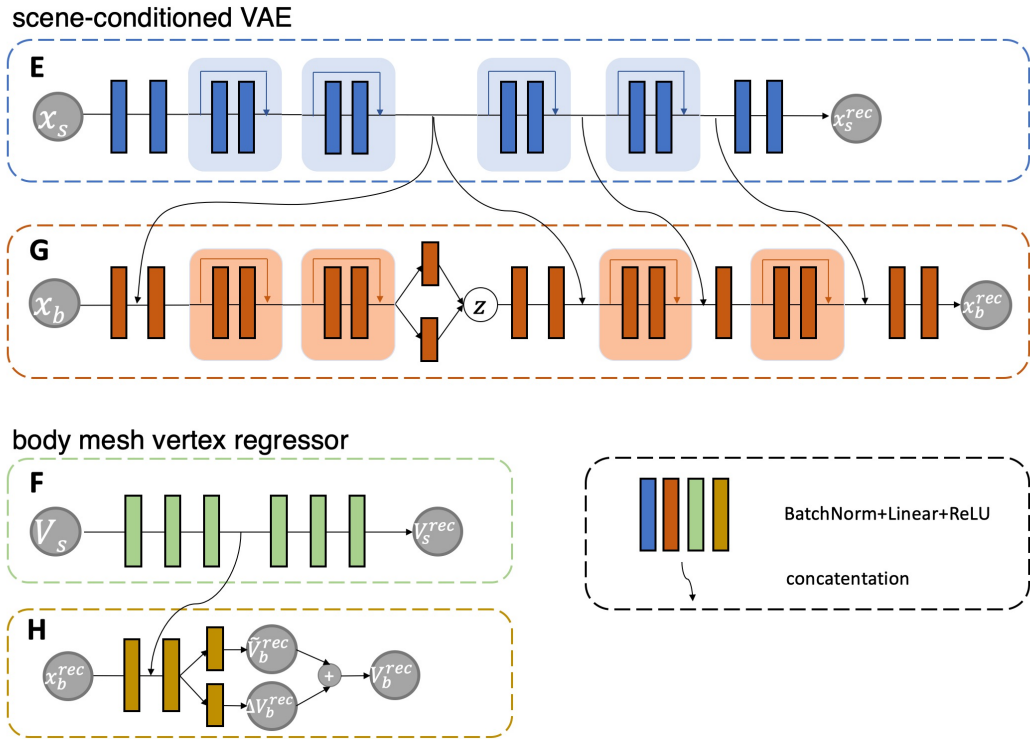


Figure S1: Architecture details.  $x_s$ ,  $\mathcal{V}_s$ ,  $x_b$  and  $\mathcal{V}_b$  denote the scene feature, the scene BPS, the body feature, and the full body mesh vertices, respectively.  $\Delta\mathcal{V}_b^{rec}$  denotes a global 3D translation.

### B. Experiment Details

#### B.1. Implementation Details

We use PyTorch [27] for implementation. We use ADAM [18] as the optimizer ( $\beta_1 = 0.9$ ,  $\beta_2 = 0.999$ ), with the learning rate 1e-4. The 3D cage size for BPS encoding (see Sec. 3.1) is set to  $2\text{m}^3$  by default. We use the same Chamfer distance implementation in the contact loss as in [6, 12, 14, 42]. The training loss weights in Eq. 1 are set as  $\alpha_1 = 0.5$ , with  $\{\alpha_2, \alpha_3\}$  set to  $\{0.001, 0.001\}$  and enabled after 75% of the training epochs. The loss weight for optimization in Eq. 6 are empirically set as  $\lambda_1 = 8$  (PROX, MP3D),  $\lambda_1 = 0.1$  (Replica),  $\lambda_2 = 0.5$ ,  $\lambda_3 = 0.02$ ,  $\lambda_4 = 0.01$ ,  $\lambda_5 = 0.01$ . The collision loss weight  $\lambda_1$  is set to a much smaller weight for Replica as the corresponding scenes are larger than PROX and MP3D, with a higher ratio of generated humans in standing poses, which seldom suffers from inter-penetration.

Table S1: **Ablation study for architecture:** we evaluate the diversity and physical metrics on the PROX dataset with different architecture variants, where **w/o ML-cat** denotes the model without multi-layer additional intermediate feature concatenation between the decoders of  $E$  and  $G$  (see Fig. 3), **w/o  $E/F$ -dec** denotes the model without decoders in  $E$  and  $F$ , **w/o  $E$**  denotes the model without  $E$ , which takes the latent vector from  $F$  into  $G$  as scene conditions,  **$H$ -S** regresses 72-d SMPL-X parameters instead of body vertices in  $H$ . All models are trained without  $\mathcal{L}_{contact}$  and collision loss  $\mathcal{L}_{coll}$  in Eq. (1).

Optimization	Model	Physical plausibility		Diversity	
		non-coll	contact	entropy	cluster size
w/o	w/o ML-cat	<b>0.95</b>	0.78	-	-
	w/o $E/F$ -dec	<b>0.95</b>	0.82	-	-
	w/o $E$	<b>0.95</b>	0.79	-	-
	$H$ -S	<b>0.95</b>	<b>0.92</b>	2.94	1.63
SimOptim	Ours	<b>0.95</b>	0.83	-	-
	w/o ML-cat	<b>0.96</b>	<b>0.84</b>	<b>2.89</b>	2.28
	w/o $E/F$ -dec	<b>0.96</b>	<b>0.84</b>	2.85	2.27
	w/o $E$	0.95	<b>0.84</b>	<b>2.89</b>	2.43
AdvOptim	Ours	<b>0.96</b>	<b>0.84</b>	<b>2.89</b>	<b>2.44</b>
	w/o ML-cat	<b>0.98</b>	0.97	2.87	2.44
	w/o $E/F$ -dec	<b>0.98</b>	0.98	2.87	2.42
	w/o $E$	0.97	0.98	2.88	2.58
	$H$ -S	0.97	<b>0.99</b>	<b>2.95</b>	1.91
	Ours	<b>0.98</b>	<b>0.99</b>	2.90	<b>2.60</b>

## B.2. Ablation Study

Here we investigate model performance from the perspectives of: (1) model architecture, (2) regressing SMPL-X parameters, and (3) 3D cage size selection.

**Model architecture.** Tab. S1 studies the following components of the proposed architecture: the additional intermediate feature concatenation between the decoders of  $E$  and  $G$  (see Fig. 3), the decoders in  $E$  and  $F$ , and the scene feature auto-encoder  $E$ . The scene BPS auto-encoder  $F$  cannot be removed as the model needs coordinate-system-dependent information to regress body vertex locations. The cluster size decreases in the absence of the first two components (w/o ML-cat and w/o  $E/F$ -dec), as these two components aim to enforce stronger scene conditioning for reconstruction and generation, hence are significant for diversity. The model without  $E$  achieves comparable scores with the full model, but we propose to encode the scene by BPS representation instead of coordinates in c-VAE due to its simplicity and independence of the coordinate system, yielding better generalization abilities.

**Regressing SMPL-X parameters.** As shown in Tab. S1, although the model regressing SMPL-X parameters ( $H$ -S) instead of body vertex coordinates achieve good contact scores, it suffers severely degraded performance w.r.t. cluster size, indicating that the generated bodies are more centralized within each cluster. Since the body mesh regressor  $H$  is conditioned on coordinates of scene BPS, regressing body vertex coordinates is an easier task than regressing SMPL-X parameters, and can learn more diverse details of body poses.

**3D cage size selection.** See results of models trained with different cage sizes in Tab. S2. One obvious pattern can be observed that the cluster size in diversity metrics increases with the cage size decreasing, which is probably because smaller cage sizes will increase randomness in global positions of the generated bodies when evaluation, since the cage is randomly cropped on test scenes. We choose the size for the 3D cage following 3 principles: 1) the size should be large enough to contain the full body in different poses, 2) the size should only include scene objects near the body, 3) the size should not be larger than training scenes, therefore we set the 3D cage size as  $2m^3$ .

Table S2: **Ablation study for 3D cage size:** the performance metrics for the model  $\text{Ours} + \mathcal{L}_{\text{contact}}$  trained with different cage sizes.

Optimization	Cage size	Physical plausibility		Diversity	
		non-coll	contact	entropy	cluster size
w/o	1.5	0.92	0.90	-	-
	2.0	<b>0.95</b>	0.90	-	-
	2.5	0.93	<b>0.95</b>	-	-
	3.0	0.92	<b>0.95</b>	-	-
SimOptim	1.5	0.93	0.95	<b>2.93</b>	<b>2.84</b>
	2.0	<b>0.96</b>	0.95	2.91	2.47
	2.5	0.93	0.95	2.92	2.26
	3.0	0.92	<b>0.96</b>	2.91	2.21
AdvOptim	1.5	0.96	0.98	<b>2.91</b>	<b>2.97</b>
	2.0	<b>0.98</b>	<b>0.99</b>	<b>2.91</b>	2.60
	2.5	0.96	<b>0.99</b>	2.88	2.44
	3.0	0.95	<b>0.99</b>	2.90	2.43

### B.3. Data Augmentation

The data preprocessing involves two different coordinate systems, i.e. the 3D cage coordinate and the unit sphere coordinate. Given a (scene, body) pair of meshes from training data, firstly the (scene, body) pair is randomly rotated around  $z$  axis of the original world coordinate. A 3D cage of  $2m^3$  is randomly selected around the body, and the scene mesh is trimmed accordingly. The (scene cage, body) vertices are rescaled by the cage size into the unit sphere, with the cage center positioned at the unit sphere center. The **3D cage coordinate** is then defined with the origin placed at the rescaled cage center. The **unit sphere coordinate** is introduced to derive the distance-based BPS features (i.e.  $\mathbf{x}_s$  and  $\mathbf{x}_b$ ), with the unit sphere center as the origin. For each training sample, the (scene cage, body) is randomly rotated around  $z$  axis of the unit sphere, and randomly shifted in a small range within the unit sphere to provide more diversity for training. Note that the point coordinates  $\mathcal{V}_s$  and  $\mathcal{V}_b$  are relative to the 3D scene cage coordinate.

With such data augmentation, the relative position between the body and 3D scene cage, and between the 3D scene cage and unit sphere will be different for each sample. This pipeline is repeated 4 times for each (scene, body) pair to enlarge the size of the training set. During inference, a 3D scene cage of the same size is randomly trimmed from the test scene.

### B.4. Details of the User Studies

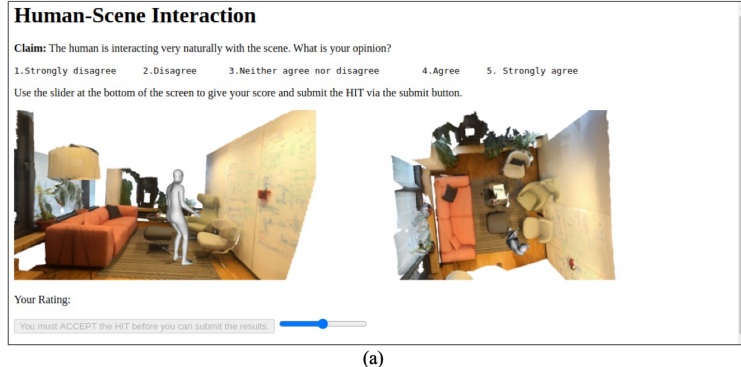
In order to evaluate the perceptual naturalness of the interactions between the generated humans and the environment, we run user study on Amazon Mechanical Turk (AMT) with two protocols: (1) unary user study, and (2) binary user study. For each scene-human pair, we display two images rendered from two different camera views to the users.

In the unary user study, each user is presented with one generation result each time, and asked to give a score between 1 (strongly not natural) and 5 (strongly natural). To alleviate randomness in the users' ratings, each result is rated by 3 users in the unary study, and we re-evaluate the baseline methods.

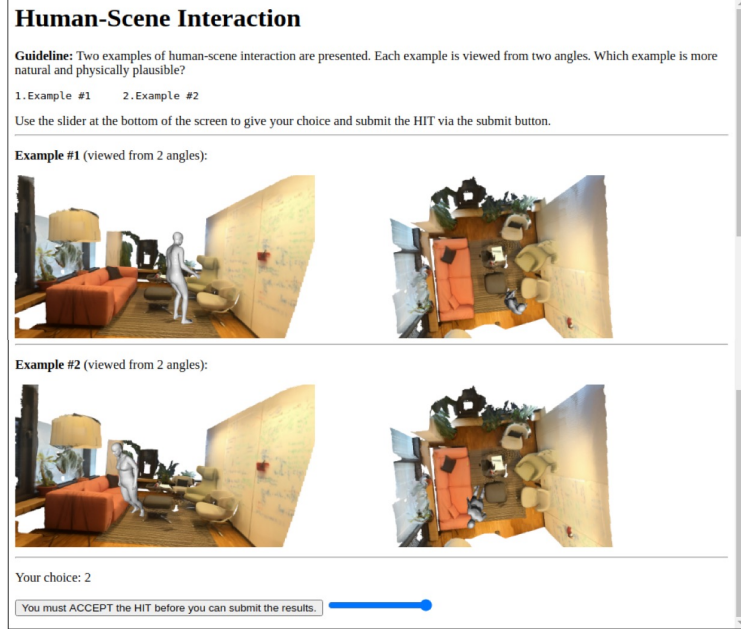
In addition, we run the binary user study to compare our method and the baseline method in [42], as well as the ground truth of PROX dataset. The users are presented with two results each time, one from the proposed method, and the other one from the baseline method or the ground truth. The user will select one which they think is more natural. The user interfaces for both unary and binary study are shown in Fig. S2.

### B.5. Examples of the SDFs for MP3D

We find that the SDFs on MP3D are not sufficiently reliable, which is probably due to noisy scans. Fig. S3 shows an example where the contact score is miscalculated as 0 by the corresponding SDF, suggesting that there is no human-scene contact, even with the obvious contact between the human and the scene (Fig. S3 (b)).



(a)



(b)

Figure S2: The user interface of the user study. (a) Unary study: the user is requested to give a score between 1 and 5 to evaluate how natural the human-scene interaction is. (b) Binary study: the user is requested to select the method in which the result is more natural.

## C. More Qualitative Results and Failure Cases

Fig. S4, Fig. S5 and Fig. S6 show qualitative results of the proposed method on test scenes of PROX, Replica and MP3D datasets respectively.

The failure cases are illustrated in Fig. S7, which can be classified into three cases. (1) The inter-penetration between the generated body before optimization is severe. Interaction-based optimization can hardly solve such case (Fig. S7 (a)) since it is non-trivial to deal with this inter-penetration case while reconstructing the generated body vertices and body features. (2) The generated body before optimization inter-penetrates with a thin structure in the scene, such as table or chair. The corresponding collision loss value in the interaction-based optimization is quite small, therefore this case can hardly be improved by the optimization (Fig. S7 (b)). (3) The generated body is floating with a small distance above the ground, or with slight inter-penetration with the scene mesh before optimization. There are two possible reasons for the floating. Firstly, there are floating bodies in the ground truth of PROX dataset, which can cause negative influences in training. Secondly, the generated body feature of the body parts in contact with the scene may not be exactly zero. The interaction-based optimization can improve the performance in this case by the contact term and collision term, respectively ((Fig. S7 (c))).



(a)

(b)

Figure S3: An example of noisy ground truth SDF from the MP3D dataset that leads to inaccurate contact metric evaluation: (a) a generated body mesh in the scene ‘17DRP5sb8fy-livingroom’ of MP3D dataset, (b) bottom-up view of the scene and body: the feet clearly have contact with the ground, however the contact score is miscalculated as 0 using the ground truth SDF.

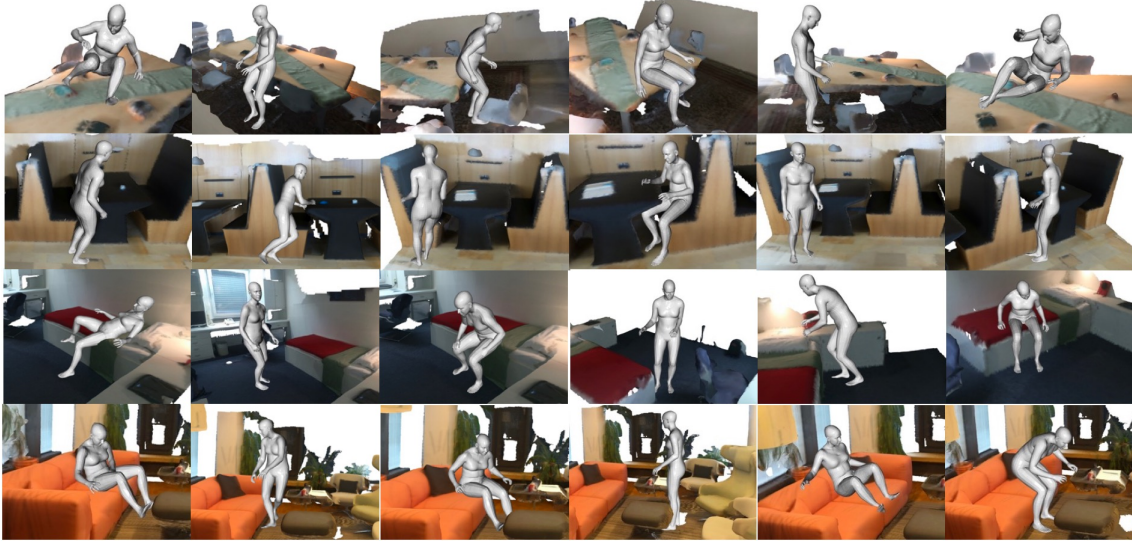


Figure S4: Qualitative results on test scenes of PROX dataset.

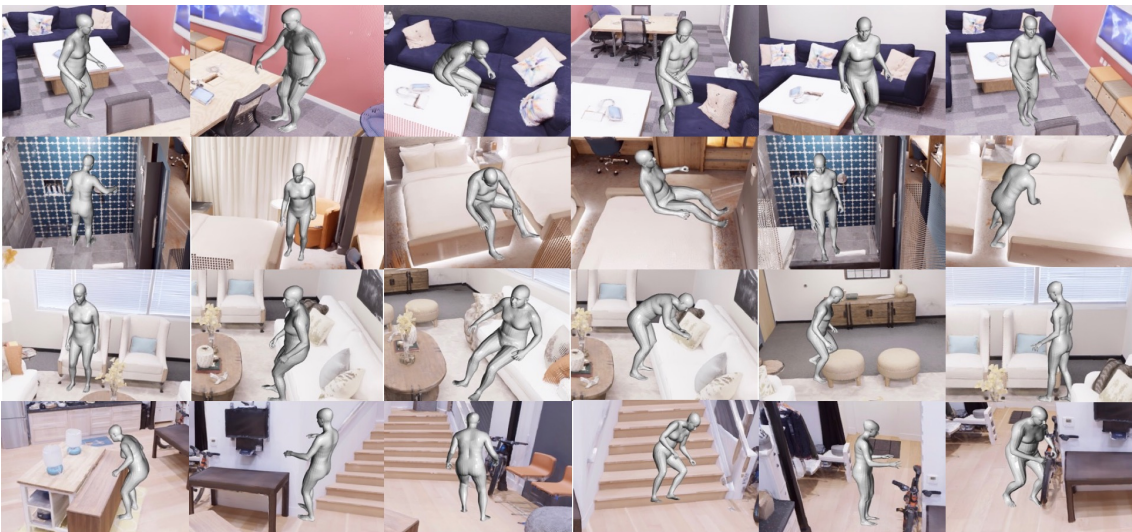


Figure S5: Qualitative results on Replica dataset.



Figure S6: Qualitative results on MP3D dataset.

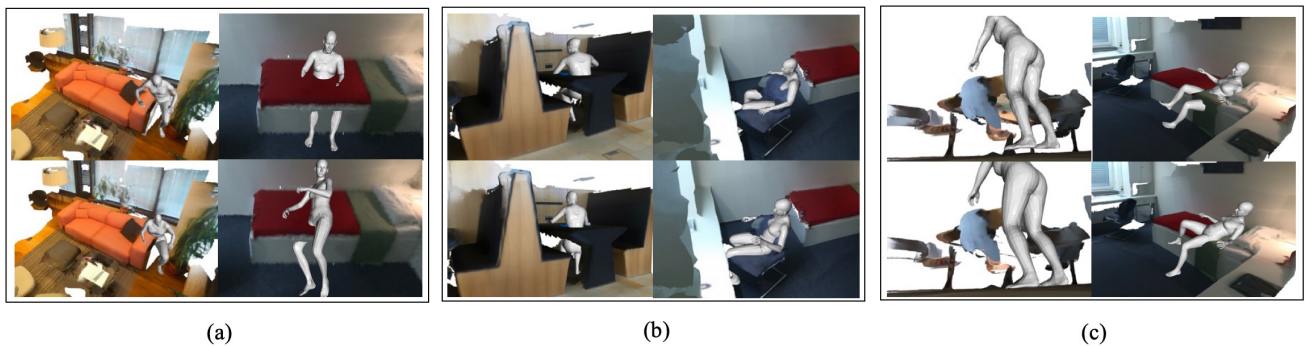


Figure S7: Failure cases: (a) severe inter-penetrations with the scene mesh, (b) inter-penetrations with thin structures in the scene and, (c) floating bodies or slight inter-penetrations with the scene mesh. The first row denotes results without interaction-based optimization, and the second row denotes results after interaction-based optimization.